# Oxidative Roles of Polystyrene Based Nanoplastics in Inducing Manganese Oxide Formation under Light Illumination

Zhenwei Gao, Ping-I Chou, Jing Liu, Yaguang Zhu, and Young-Shin Jun\*

Department of Energy, Environmental and Chemical Engineering, Washington University in St. Louis, St. Louis, Missouri 63130, United States

Address: One Brookings Drive, Campus Box 1180

E-mail: ysjun@seas.wustl.edu

Phone: (314) 935-4539

Fax: (314) 696-1223

http://encl.engineering.wustl.edu/

## ACS Nano

Submitted: June 2022

Revised: October 2022

\* To whom correspondence should be addressed

1 ABSTRACT: Every year, large quantities of plastics are produced and used for diverse 2 applications, growing concerns about the waste management of plastics and their release into the 3 environment. Plastic debris can break down into millions of pieces that adversely affect natural 4 organisms. In particular, the photolysis of micro/nanoplastics can generate reactive oxygen species 5 (ROS). However, their oxidative roles in initiating redox chemical reactions with heavy and 6 transition metals have received little attention. In this study, we investigated whether the photolysis 7 of polystyrene (PS) nanoplastics can induce the oxidation of Mn<sup>2+</sup>(aq) to Mn oxide solids. We 8 found that PS nanoplastics not only produced peroxyl radicals (ROO') and superoxide radicals 9 (O2<sup>•</sup>) by photolysis, which both play a role in unexpected Mn oxidation, but also served as a 10 substrate for facilitating the heterogeneous nucleation and growth of Mn oxide solids and 11 controlling the formation rate and crystalline phases of Mn oxide solids. These findings help us to 12 elucidate the oxidative roles of nanoplastics in the oxidation of redox-active metal ions. The 13 production of ROS from nanoplastics in the presence of light can endanger marine life and human 14 health, and affect the mobility of the nanoplastics in the environment via redox reactions, which 15 in turn may negatively impact their environmental remediation.

- 16 **KEYWORDS:** nanoplastics; photochemistry; abiotic Mn<sup>2+</sup> oxidation; heterogeneous nucleation;
- 17 peroxyl radicals; superoxide radicals

#### INTRODUCTION

18

19

20

21

22

23

24

25

26

27

28

29

30

31

32

33

34

35

36

37

38

39

40

Plastics have become widely used in the last 70 years owing to their light weight, durability, versatility, and low cost. <sup>1-3</sup> The global production of primary plastics has grown rapidly, increasing from 2 million tons (Mt) per year in 1950 to 407 Mt per year in 2015.<sup>3</sup> According to Geyer et. al (2017), 8,300 Mt of virgin plastics were estimated to be produced by 2015, ultimately generating 6,300 Mt of plastic wastes.<sup>3</sup> Alarmingly, only about 9% of these wastes were recycled, 79% were discarded in the environment or landfilled, and the rest were incinerated.<sup>2, 3</sup> Plastic wastes have also become common and persistent pollutants in oceans worldwide. Among many different types of plastics, the most common in the marine environment are polyethylene terephthalate (PET), polyethylene (PE), polyvinyl chloride (PVC), polypropylene (PP), and polystyrene (PS).<sup>4</sup> Plastic products usually last for tens or even hundreds of years before their complete degradation.<sup>5</sup> UV irradiation, 6 mechanical breakdown, 7,8 and biological breakdown 9 can make a single large plastic piece fragile and break it into millions of small pieces, <sup>10, 11</sup> including macroplastics (> 5 mm), <sup>11</sup> microplastics (100 nm-5 mm), <sup>12</sup> and nanoplastics (1-1000 nm)<sup>13</sup>. Larger pieces of plastic debris can harm fish, birds, and marine mammals in aquatic ecosystems by entanglement and ingestion. <sup>14</sup>, <sup>15</sup> In addition, microplastics and nanoplastics can be ingested by small organisms, such as zooplankton, 16 which will further affect marine food webs. Moreover, compared with the original plastic pieces, the smaller sizes of degraded/broken plastics have significantly larger specific surface areas, <sup>17</sup> so they can interact with surrounding environmental compounds much more easily, be co-transported and transformed, and be aggregated in aqueous environments. 10, 17

When plastics are released into the environment, they interact with diverse aqueous substances. Previous studies have revealed that plastics adsorbed heavy metal ions, such as  $Pb^{2+}$ ,  $Cu^{2+}$ ,  $Ni^{2+}$ ,  $Zn^{2+}$ , and  $As^{3+}$ ,  $I^{18-21}$  and organic pollutants, such as bisphenol A (BPA),

dichlorodiphenyltrichloroethane (DDT), and polychlorinated biphenyls (PCBs).<sup>22-26</sup> In addition to adsorption, recent studies have started to investigate plastics as a source for reactive oxygen species (ROS) under light illumination. Sunlight can trigger the degradation and transformation of plastics in the environment. During the photolysis of microplastics, ROS, including superoxide radicals (O2<sup>+</sup>), hydroxyl radicals (\*OH), singlet oxygen (<sup>1</sup>O<sub>2</sub>), and hydrogen peroxide (H<sub>2</sub>O<sub>2</sub>),<sup>27, 28</sup> can be generated, while endogenous pollutants, such as chemical additives and polymer fragments, are leached out.<sup>6, 29, 30</sup> Similarly, the photolysis of PS-based nanoplastics can generate \*OH, <sup>1</sup>O<sub>2</sub>, and O2<sup>+-,31</sup> Tian *et al.* (2019) and Wang *et al.* (2020) proposed that alkyl radicals (R\*) and peroxyl radicals (ROO\*) trigger the formation of the above ROS, but the presence of these two radicals was not experimentally examined.<sup>31, 32</sup> These findings highlight the potential strong oxidative roles of plastics in natural environments.

To date, the oxidative roles of nanoplastics in inducing redox reactions with heavy or transition metals remain uninvestigated. During sunlight irradiation of nanoplastics, the generation of ROS could also affect the redox reactions of heavy metals and the formation of corresponding metal oxides. For example, manganese (Mn) is a naturally abundant transition metal, and Mn (hydr)oxides are some of the most reactive natural minerals, with excellent oxidation and adsorption capabilities. Thus, Mn oxides affect the biogeochemical cycles of trace elements, metal ions, and organics in the environment.<sup>33-35</sup> Mn<sup>2+</sup> was also found to adsorb on the surface of microplastics from the beach.<sup>36</sup> Recently, we reported photochemically assisted abiotic oxidation of Mn<sup>2+</sup>(aq) to Mn(IV) by O2<sup>\*-</sup> during nitrate photolysis,<sup>37</sup> and by ROO\* in the presence of additional *tert*-butyl alcohol.<sup>38</sup> These works suggested abiotic pathways to generate Mn(IV) oxide solids directly from Mn<sup>2+</sup>(aq), whereas the biotic oxidation of Mn<sup>2+</sup>(aq) was previously believed to be the main mechanism of Mn oxidation from 2+ to 4+.<sup>34,39-43</sup> Our previous studies investigated

the homogeneous nucleation and growth of Mn(IV) oxide solids—particle formation in solution.<sup>37, 38</sup> However, in the presence of nanoplastics, heterogeneous nucleation—particle formation on a substrate—can occur on the nanoplastics' surface in the environment. Based on these recent findings of Mn oxidation, in the current study, we hypothesized that the ROS generated from the photolysis of nanoplastics can trigger the oxidation of Mn<sup>2+</sup>(aq) to Mn oxide solids. Because nanoplastics were reported to work as substrates for microorganisms, leading to the formation of biofilm, <sup>11</sup> we further hypothesized that heterogeneous nucleation and growth of Mn oxide solids would occur on the surface of nanoplastics. Compared with homogeneous nucleation without substrates, plastics can decrease the activation energy barrier of heterogeneous nucleation of Mn oxide nanoparticles, affecting the crystalline phases of the formed Mn oxide. Subsequently, this reaction process can influence the redox reaction behaviors and phase transformation of newly formed Mn oxide solids. Moreover, it is unknown how the material properties of nanoplastics, such as their particle sizes and functional groups, affect Mn<sup>2+</sup> oxidation.

This study shows how the photolysis of nanoplastics can initiate the oxidation of Mn<sup>2+</sup>(aq) to Mn(IV) oxide solids and confirms the formation of ROO\* and O2\* as the radicals mainly responsible for Mn oxidation. We selected spherical PS-based nanoplastics as the nanoplastic model. We verified the production of ROO\* and O2\* during photolysis of PS nanoplastics and observed Mn oxidation by these radicals. We also investigated how the different sizes (30, 100, and 500 nm) and functional groups of polystyrene latex beads (PS-bare), carboxylate-modified polystyrene latex beads (PS-COOH), and amine-modified polystyrene latex beads (PS-NH<sub>2</sub>) affected Mn oxidation. We observed different mineral phases of Mn oxide solids from heterogeneous nucleation on nanoplastics, distinct from those from homogeneous nucleation of Mn oxide solids *via* nitrate photolysis. These findings fill in knowledge gaps in the oxidative roles

- 87 of nanoplastics in the generation of ROS and the subsequent oxidation of transition metal ions.
- 88 This work also provides helpful insights into the oxidation of other redox-active metal ions (e.g.,
- 89 Fe<sup>2+</sup>, As<sup>3+</sup>, and Cr<sup>3+</sup>), and the heterogeneous formation of Mn oxide solids on organic substrates,
- 90 such as plastic wastes.

91

92

93

94

95

96

97

98

99

100

101

102

103

104

105

106

107

108

109

#### RESULTS AND DISCUSSION

Effects of pH, Particle Sizes, and Chemical Functional Groups of Nanoplastics on Mn<sup>2+</sup> **Oxidation.** Figure 1a schematically illustrates the photolytic experiment in which Mn oxide solids formed in the presence of PS-based nanoplastics. We investigated whether the photolysis of PS nanoplastics can initiate the oxidation of  $Mn^{2+}$  (aq) and studied the effect of pH on  $Mn^{2+}$  oxidation. First, the pH effect was tested because we found in our previous study that solution pH greatly affected Mn<sup>2+</sup> oxidation.<sup>37, 38</sup> As shown in Figure 2a,b, two solutions containing 0.1 mM manganese chloride (MnCl<sub>2</sub>) and 10 ppm (mg/L) of 30 nm PS-COOH were prepared, one with and the other without a pH buffer (10 mM borate buffer). Both solutions were adjusted to initial pH 9. During the photolysis experiments, the pH of the unbuffered solution decreased from 9 to 7.5 in 1 hr and steadily dropped to pH 7 from 1 to 6 hr, and Mn oxidation mostly occurred within 1 hr (pH > 7.5). In our previous work, we explained that the solution pH decreased mainly due to the formation of Mn oxide solids. 44 In addition, CO<sub>2</sub> dissolution into the solution can also decrease pH. 44 Without a buffer, the concentration of formed Mn oxide solids was  $3.3 \pm 0.3 \mu M$  (based on Mn(IV) oxidation state) and almost reached a plateau at 1hr. It slightly increased to  $4.1 \pm 0.2 \mu M$ from 1 to 6 hr. On the other hand, with 10 mM borate buffer, Mn oxidation kept increasing in the experimental solution. The concentration of formed Mn oxide solids was about  $47.1 \pm 1.9 \,\mu\text{M}$  at 6 hr. The pH remained at  $8.9 \pm 0.1$  during the 6 hr experiment. In contrast, Mn oxidation was not observed under the dark condition of the above solution, as shown in Figure S1a. As shown in

Figure S1b, a negligible amount of Mn oxidation was observed in a solution containing 0.1 mM MnCl<sub>2</sub> and 10 mM borate buffer without nanoplastics under illumination. The above results indicated that the Mn<sup>2+</sup> was more preferably oxidized at a pH higher than 7.5 during the photolysis of nanoplastics.

In addition, as purchased, polystyrene latex beads will contain very small amounts of surfactant and inorganic salts. To control for this, a solution containing 10 ppm of 500 nm PS-COOH was filtered by a 0.2 µm polytetrafluoroethylene (PTFE) syringe filter for three times to remove all PS-COOH nanoplastics from the solution. The filtered solution containing surfactant and inorganic salts was used to investigate their effects on Mn oxidation. As seen in Figure S1b, an insignificant amount of Mn oxidation (< 1 µM) was observed under the condition of 0.1 mM MnCl<sub>2</sub>, 10 mM borate buffer, and 10 ppm of 500 nm PS-COOH filtered by 0.2 µm PTFE syringe filter under illumination, indicating that the surfactant and inorganic salts play little roles in Mn oxidation.

Next, we investigated the effects of the nanoplastic size on  $Mn^{2+}$  oxidation. Three different sizes of PS-COOH particles (30, 100, and 500 nm) were selected for comparison. As shown in Figure 2c, compared with 30 nm PS-COOH particles, 100 and 500 nm PS-COOH nanoplastic particles needed a longer induction time for Mn oxidation because slower  $Mn^{2+}$  oxidation rates were observed with the larger PS-COOH particle sizes. In solutions with the same mass concentration (10 ppm), smaller nanoplastic particles in the solution outnumbered larger ones and had a correspondingly larger total surface area. In this study, we assumed that all the nanoplastics were spherical particles, as shown in Figure 4a and Figure S2a, with a density of  $1.05g/cm^3$ , which is the density of polystyrene. In 150 mL of 10 ppm PS-COOH solution, PS-COOH particles had a total volume of  $1.43 \times 10^{18}$  nm<sup>3</sup>. For 30, 100, and 500 nm PS-COOH particle solutions, the corresponding surface areas were  $2.86 \times 10^{17}$  nm<sup>2</sup>,  $8.57 \times 10^{16}$  nm<sup>2</sup>, and  $1.71 \times 10^{16}$  nm<sup>2</sup>. Thus,

smaller-sized nanoplastics exposed relatively larger specific surface areas with more functional groups to initiate ROS production during the photolysis, resulting in more and much faster Mn oxidation. In addition, because of their larger specific surface area, the smaller particle size of PS-COOH nanoplastics may more easily decompose and release organic matter. The dissolved organic matter may produce ROS under illumination and facilitate Mn oxidation, as reported in our previous study. 44 Hence, the trend of the Mn oxidation rate for 30 nm PS-COOH was different from those of 100 and 500 nm PS-COOH. In Figure 2c, the ratio of the Mn oxidation amounts for 30 nm to 500 nm PS-COOH was not exactly linearly correlated with the ratio of the total surface areas. The Mn oxidation amount for 30 nm PS-COOH reached a plateau from 4 to 6 hr; however, Mn oxidation still increased under the 100 nm or 500 nm PS-COOH condition. One reason may be that most of the particles of 30 nm PS-COOH were covered by Mn oxide solids at 6 hr, which limited further Mn oxidation, while 100 nm PS-COOH nanoparticles were not fully covered, as shown in the TEM images in Figure 4c and Figure S2b. Mn oxide formation on the surface of the nanoplastics blocked illumination and inhibited ROS generation, which can explain why Figure 2c shows that Mn oxidation almost reached a plateau after 4 to 6 hr in the 30 nm PS-COOH solution, but continued in the 100 nm PS-COOH solution: The larger particles were less completely blocked by Mn oxides. Furthermore, we found that the kinetics of Mn<sup>2+</sup> oxidation were affected by the functional

133

134

135

136

137

138

139

140

141

142

143

144

145

146

147

148

149

150

151

152

153

154

155

Furthermore, we found that the kinetics of Mn<sup>2+</sup> oxidation were affected by the functional groups of nanoplastics. We compared Mn<sup>2+</sup> oxidation rates by using PS-bare, PS-COOH, or PS-NH<sub>2</sub> nanoplastics with the same size (100 nm) and mass concentration (10 ppm). As shown in Figure 2d, the quantity of generated Mn oxide solids decreased in the order of PS-NH<sub>2</sub> > PS-COOH > PS-bare. The pH values of the solutions for all conditions remained around pH 9 (Figure 2b), thus the pH cannot be the reason for the difference. The various amounts of Mn oxide solids

generated by different functional groups of nanoplastics might result from the different generation rates of ROS responsible for Mn<sup>2+</sup> oxidation (ROO\* and O2\*-), as discussed in the next section.

Pathways for Generating ROO' and O2'—during Photolysis of Nanoplastics. In this study, we propose that ROO' and O2'— are generated by the photolysis of PS-based nanoplastics, which can further play a role in Mn oxidation (Figure 1). Previous studies found that ROS, such as 'OH, <sup>1</sup>O2, and O2'—, can be produced during the photolysis of micro/nanoplastics. Zhu *et al.* (2020) measured the generation of O2'—, <sup>1</sup>O2, H2O2, and 'OH from the photo-transformation of PS microplastic powders in water under simulated sunlight irradiation. <sup>28</sup> In another study, Wang *et al.* (2020) detected the formation of 'OH, <sup>1</sup>O2, and O2'— by electron spin resonance spectrometry during the photo-oxidation of PS-based nanoplastics and proposed that R' and ROO' could be potentially responsible. <sup>31</sup> However, the generation of ROO' was not experimentally proved.

For the generation of ROO', as shown in Figure 1b, PS-bare, PS-NH<sub>2</sub>, and PS-COOH transform to R' by photolysis (**Step I**), and subsequently transform to ROO' by reacting with dissolved O<sub>2</sub> (**Step II**). <sup>31, 32, 45, 46</sup> For PS-bare, the α C-H close to the phenyl group was much more easily broken by the energy transfer from phenyl absorption. <sup>45, 46</sup> R' can also transform to 'OH by reacting with H<sub>2</sub>O (**Step III**). <sup>32</sup> The bond dissociation energies of the monomers C<sub>6</sub>H<sub>5</sub>CH<sub>2</sub>-H (PS-bare), C<sub>6</sub>H<sub>5</sub>CH<sub>2</sub>-NH<sub>2</sub> (PS-NH<sub>2</sub>), and C<sub>6</sub>H<sub>5</sub>CH<sub>2</sub>-COOH (PS-COOH) are 360, 301, and 284.9 kJ/mol, respectively. <sup>47, 48</sup> The differences in the bond dissociation energies can affect the generation of R' and ROO'. Among these three nanoplastics with different functional groups, PS-bare would have the most difficulty in forming R' owing to the highest bond dissociation energy, thus generating the least amount of ROO'. On the other hand, the bond dissociation energy difference between PS-COOH and PS-NH<sub>2</sub> is not significant. This reasoning can explain the lowest generated amount of Mn oxide solids by photolysis of PS-bare in Figure 2d.

 $O_2$  can be produced by multiple pathways, as shown in Figure 1c. Dissolved  $O_2$  can transform to  $O_2$  by electron transfer. O<sub>2</sub> can also be produced when OH formed from photolysis of nanoplastics reacts with  $H_2O_2$  to form  $HO_2$ , which is then further transformed to  $O_2$ .

Thus, in the next section, we will experimentally confirm that both ROO' and O2<sup>--</sup> are formed by the photolysis of nanoplastics, causing Mn<sup>2+</sup> oxidation in our experimental systems. In addition to PS-bare, PS-COOH, and PS-NH<sub>2</sub>, other functional groups (e.g., PS-sulfate) may cause Mn<sup>2+</sup> oxidation through a similar photolytic mechanism. Manufactured nanoplastics can contain hydroperoxide (R-OOH) polymer impurities, which can generate carbon-centered radicals and further form ROO'.<sup>50, 51</sup> To check for hydroperoxide impurities in the nanoplastics, the PS-bare nanoplastics stock solution was dried on a Si wafer and measured by FTIR, as shown in Figure S3. Peaks related to R-OOH in the range from 3450-3350 cm<sup>-1</sup> were not observed, <sup>52, 53</sup> indicating that R-OOH impurities were ignorable.

Detection of the Generation of ROO\*. The formation of ROO\* was confirmed to validate the proposed radicals' formation pathways. To detect the formation of ROO\*, the fluorescent probe *para*-aminobenzoic acid (PABA) was used, as in our previous work.<sup>38</sup> Here ROO\* can oxidize and transform PABA into a non-fluorescent product, and thus we can quantify ROO\*.<sup>54</sup> Note that the oxidation potential of PABA is higher than those of O2\*, <sup>1</sup>O2, and H2O2.<sup>54,55</sup> Based on our previous work,<sup>38</sup> O2\*, <sup>1</sup>O2, and H2O2 generated from photolysis of nitrate cannot oxidize PBBA. We have also shown that 'OH has little effect on PABA oxidation.<sup>38</sup> Therefore, we expected that all of these ROS (O2\*, <sup>1</sup>O2, H2O2, and 'OH) would not affect the oxidation of PABA. However, PABA can be photodegraded, and the reaction is highly pH-dependent.<sup>56</sup> Hence, to maintain the solution pH, borate buffer was used in the experiment. Two solutions containing 20 μM PABA and 10 mM borate buffer, one with and the other without 50 ppm of 100 nm PS-NH2, were irradiated. As shown

in Figure 3a, the percentages of PABA concentrations decrease with time. After 5 min reaction, photodegradation is responsible for a  $30.0 \pm 3.2\%$  PABA concentration decrease. In the presence of 50 ppm of 100 nm PS-NH<sub>2</sub>, even faster PABA degradation was observed, with a  $39.3 \pm 1.1\%$  PABA concentration decrease after 5 min owing to the co-effects of photodegradation and ROO oxidation. Notably, the presence of nanoplastics in the solution had shadowing effects on the photodegradation of PABA by blocking light exposure, which inhibited the PABA photodegradation rate. The photodegradation rate of PABA in the presence of nanoplastics was supposed to be slower than that in the absence of nanoplastics. As a result, the actual contribution of ROO for PABA degradation could have been greater than the degradation difference between with- and without-nanoplastics in Figure 3a. In addition, because the solution pH was stable during photolysis, as shown in Figure S4a, we ruled out the solution pH as a factor in the PABA photodegradation results. The above results confirmed the generation of ROO during the photolysis of nanoplastics.

Mn<sup>2+</sup> Oxidation by ROO<sup>+</sup> and O<sub>2</sub><sup>--</sup>. Our earlier work found that compared with O<sub>2</sub><sup>--</sup> and ROO<sup>+</sup>, OH contributed much less to Mn oxidation in our systems.<sup>37, 38, 57</sup> H<sub>2</sub>O<sub>2</sub> was regarded as a reductant for Mn oxide solids, so we did not expect that it played a direct role in Mn oxidation. Nico *et al.* (2002) reported Mn oxidation by O<sub>2</sub><sup>+-</sup> and <sup>1</sup>O<sub>2</sub> from photolysis of humic substances, however, <sup>1</sup>O<sub>2</sub> oxidized Mn<sup>2+</sup> to Mn(III), but not to Mn(IV) oxide solids, so and only 4% of the formed Mn(III) came from <sup>1</sup>O<sub>2</sub>, while the other 96% came from O<sub>2</sub><sup>+-</sup>. Thus, <sup>1</sup>O<sub>2</sub> was unlikely to contribute much to the generation of Mn oxide solids in our study, and O<sub>2</sub><sup>+-</sup> and ROO<sup>+</sup> were considered as the main oxidants of Mn<sup>2+</sup> during the photolysis of PS-based nanoplastics.

We have confirmed the formation of ROO from the photolysis of nanoplastics in the last section. To validate that the production of ROO and O2 from the photolysis of nanoplastics

induced Mn<sup>2+</sup> oxidation and to investigate their individual contribution to Mn<sup>2+</sup> oxidation, superoxide dismutase (SOD) was used as an O2<sup>+-</sup> scavenger. Two solutions containing 0.1 mM MnCl<sub>2</sub>, 10 ppm of 30 nm PS-COOH, and 10 mM borate buffer, were prepared, one with and the other without 0.5 μM SOD. In the presence of SOD, less Mn oxidation was observed, as shown in Figure 3b, indicating that O2<sup>+-</sup> was formed during the photolysis of PS-COOH and was responsible for Mn<sup>2+</sup> oxidation. Mn<sup>2+</sup> can react with O2<sup>+-</sup> and H<sup>+</sup> to form Mn<sup>3+</sup> and H<sub>2</sub>O<sub>2</sub>.<sup>60</sup> In the presence of SOD, we think Mn<sup>2+</sup> was mainly oxidized by ROO<sup>+</sup>. Similar to O2<sup>+-</sup>, ROO<sup>+</sup> might react with H<sup>+</sup>, be converted to R-OOH, and oxidize Mn<sup>2+</sup>. Again, pH was not a factor in the different Mn oxidation results with/without SOD because it remained the same, as shown in Figure S4b.

We also investigated the individual contributions to Mn oxidation by ROO\* and O2\* generated from different particle sizes of PS-COOH and PS with other functional groups (PS-NH<sub>2</sub> and PS-bare). As shown in Figure S5, in the presence of SOD, compared with PS-bare, more Mn oxidation was observed by ROO\* from 100 nm PS-NH<sub>2</sub> and PS-COOH, which might result from the highest bond dissociation energy for PS-bare as explained earlier. In addition, the difference in MnO<sub>2</sub> concentration with/without SOD was the Mn<sup>2+</sup> oxidation amount by O2\*. More Mn<sup>2+</sup> oxidation was observed by O2\* from 100 nm PS-NH<sub>2</sub>, compared with PS-COOH and PS-bare.

Notably, we found that N in PS-NH<sub>2</sub> was oxidized during the photolysis of PS-NH<sub>2</sub>, as shown in Figure 3c,d, where 50 ppm of 100 nm PS-NH<sub>2</sub> underwent photolysis for 12 hr. In Figure 3c, compared with PS-NH<sub>2</sub> before photolysis, the peak of the N1s X-ray photoelectron spectra in PS-NH<sub>2</sub> after photolysis moved to higher energy (402.7 eV), possibly resulting in the photooxidation of -NH<sub>2</sub> to -NO<sub>2</sub>.<sup>61</sup> In Figure 3d, the weakness of the peak from N-H bending at 1602 cm<sup>-1</sup> after photolysis also confirmed the oxidation of N in PS-NH<sub>2</sub>. As shown in Figure 3e, the photolysis of R-NO<sub>2</sub> can produce nitrite.<sup>62</sup> During the photolysis of nitrite, ROS, including O<sub>2</sub>\*- and \*OH, can

also be generated.<sup>63</sup> In the previous studies,<sup>37, 57</sup> we observed the facilitated oxidation of Mn<sup>2+</sup> by O<sub>2</sub><sup>--</sup> during nitrate photolysis, and explained that nitrite was an intermediate for forming O<sub>2</sub><sup>--</sup>. As illustrated in Figure S5a, the possible generation of nitrite during photolysis of PS-NH<sub>2</sub> could provide a potential mechanism that explains why more Mn<sup>2+</sup> oxidation by O<sub>2</sub><sup>--</sup> was observed from 100 nm PS-NH<sub>2</sub> than from PS-COOH and PS-bare. As for PS-COOH, the COOH group transforms to CO<sub>2</sub> or other products during photolysis rather than generating radicals that are responsible for Mn oxidation.<sup>64, 65</sup>

Other intermediate radicals also can form in the chain reactions during the photolysis of nanoplastics. For example, ROO can transform into alkoxy radicals (RO) and further decompose into other radicals. However, it is unknown whether these intermediate radicals can oxidize Mn<sup>2+</sup>. Further, these radicals can swiftly change into other radicals, high which makes it difficult to study the sole contribution of each intermediate species for Mn<sup>2+</sup> oxidation. The role of each intermediate radical in Mn<sup>2+</sup> oxidation needs to be determined more systematically in the future.

Heterogeneous Nucleation of Mn Oxides on the Nanoplastics. We also investigated the morphologies of formed Mn oxide solids on 30 or 100 nm PS-COOH nanoplastics. Scanning transmission electron microscope (STEM) revealed their sizes, shapes, and elemental compositions. As shown in Figure 4b,c, rod-shaped Mn oxide solids formed on the surface of PS-COOH. ROO\* and O2\* both have very long lifetimes (seconds for ROO\*, and microseconds for O2\*),68,69 which might allow them to participate in the oxidation of Mn²+ over a long distance. Thus, long rod-shaped Mn oxides can grow around and beyond the surface of PS-COOH (Figure 4c). The diameter of the PS-COOH is slightly smaller than 100 nm (Figure 4a). The element mapping of O, Mn, and C in Figure 4d–f, collected from Figure 4c, confirms the formation of Mn oxide solids. The selected area electron diffraction (SAED) patterns in Figure 4g indicate that the

rod-shaped Mn oxide solids in Figure 4c are α-MnO<sub>2</sub>. The Mn and C element mapping images collected from the dash area in Figure 4b overlap in Figure 4i, clearly showing that the Mn oxide solids formed surrounding 100 nm PS-COOH nanoplastics. As Figure 4c shows, 100 nm PS-COOH nanoplastics are only partially covered by Mn oxide solids after 6 hr reaction. In stark contrast, with 30 nm PS-COOH nanoplastics (Figure S2a–c), significantly densely packed rod-shaped Mn oxide solids were formed. The element mapping images of Mn, O, and C in Figure S2d–f were collected from Figure S2b. It is hard to see the 30 nm PS-COOH nanoplastic particles, because most of them are fully covered by formed Mn oxide solids, except for the particles near the edge.

The hydrodynamic diameters of the nanoplastics were measured by dynamic light scattering to provide additional evidence for the heterogeneous nucleation and growth of Mn oxide solids on them. As shown in Figure S6a, under illumination the hydrodynamic diameter of  $\sim$ 100 nm PS-COOH did not change without Mn<sup>2+</sup>. However, with Mn<sup>2+</sup>, it increased from 112  $\pm$  1 nm to 138  $\pm$  1 nm during 2 hr reaction, indicating the nucleation and growth of Mn oxide solids on the surface of the PS-COOH nanoplastics. For comparison, the hydrodynamic diameter remained the same size in the dark condition, because no Mn oxide solids were formed. The initial hydrodynamic diameter of PS-COOH without Mn oxide solids was larger than that in the STEM image in Figure 4a because the hydrodynamic diameter includes tightly bound water molecules. The zeta potential values of nanoplastics were also measured to study the effects of surface potential on the interactions between Mn<sup>2+</sup> and nanoplastics. In Figure S6b, initially, the zeta potential values of 10 ppm of 100 nm PS-COOH nanoplastics were about -42.3  $\pm$  0.3 mV in solutions containing 10 mM borate buffer solution without Mn. After 2 hr of illumination, the zeta potential value remained between -42 and -43 mV. In contrast, the zeta potential values of 10 ppm of 100 nm PS-COOH

nanoplastics were initially about  $-39.2 \pm 0.4$  in the solution containing 10 mM borate buffer and 0.1 mM MnCl<sub>2</sub>. With reaction under 2 hr light illumination, the zeta potential value increased from  $-39.2 \pm 0.4$  to  $-37.3 \pm 0.1$  mV. The Mn oxide solids formed on the surface of the nanoplastics would make the zeta potentials less negative than that of unreacted PS-COOH. On the other hand, the hydrodynamic diameter of 100 nm PS-NH<sub>2</sub> nanoplastics increased from  $96 \pm 2$  nm to  $137 \pm 1$ nm in 2 hr, as shown in Figure S6c. The growth rate of PS-NH<sub>2</sub> was faster than that of PS-COOH, which was consistent with the result that more Mn oxide solids were formed in PS-NH2 than in PS-COOH, as shown in Figure 2d. Different from PS-COOH (Figure S6d), PS-NH<sub>2</sub> nanoplastics initially had positive zeta potential values of 15.5  $\pm$  1.0 mV and 12.2  $\pm$  0.7 mV in solutions containing 10 mM borate buffer without Mn and 10 mM borate buffer with 0.1 mM MnCl<sub>2</sub>, respectively. After 2 hr of illumination, the zeta potential value of PS-NH<sub>2</sub> in the formed solution remained at  $15.5 \pm 1.0$  mV, while in the latter solution it decreased from  $12.2 \pm 0.7$  to  $9.0 \pm 0.5$ mV after 2 hr owing to the negative zeta potential contribution from newly formed Mn oxide solids on the surface. As an additional note, without nanoplastics, Mn(IV) oxide solids generated by nitrate photolysis in pH 9 borate buffer had a negative zeta potential value of  $-24.2 \pm 0.6$  mV. Both the increase in the hydrodynamic diameters and the change in the zeta potential values of the nanoplastics confirmed the formation of Mn oxide solids on their surface.

294

295

296

297

298

299

300

301

302

303

304

305

306

307

308

309

310

311

312

313

314

315

316

Characterization of MnO<sub>2</sub> Solids Formed on the Nanoplastics. To characterize the crystalline phases of the Mn oxide solids formed by the photolysis of nanoplastics with different sizes and functional groups, samples after 6 hr reaction were measured by high-resolution X-ray diffraction (HRXRD). As shown in Figure 5a, a 2θ peak value of 18.1° for Mn oxide solids formed by 100 nm PS-COOH, PS-NH<sub>2</sub>, or PS-bare nanoplastics indicated that α-MnO<sub>2</sub> (ICDD PDF-4 #00-042-1348) had formed as the dominant crystalline phase. On the other hand, in the 30 nm PS-

COOH system, amorphous XRD patterns were observed, although much more Mn oxide solids were produced by 30 nm PS-COOH, compared with 100 nm PS-COOH and PS-NH<sub>2</sub>. The large surface area of an individual large nanoplastic particle may better support the orientated growth of Mn oxides and stabilize the newly formed Mn oxides, resulting in a more crystallized structure. The broad peak ranging from 18° to 20° includes a small peak of the (200) plane of α-MnO<sub>2</sub> and can also be consistent with the (111) plane of  $\lambda$ -MnO<sub>2</sub> (ICDD PDF-4 #00-044-0992); however, the patterns of 30 nm PS-COOH sample were too amorphous to distinguish. Mn oxides solids formed by 100 nm PS-COOH and 100 nm PS-bare also exhibit small peaks in this range. Thus, Mn oxide solids formed in 30 nm PS-COOH, 100 nm PS-COOH, or 100 nm PS-bare solutions might contain both  $\alpha$ -MnO<sub>2</sub> (dominant) and  $\lambda$ -MnO<sub>2</sub>. In a previous study, we observed the formation of  $\delta$ -MnO<sub>2</sub> by  $O_2^{\bullet-}$  during nitrate photolysis in the absence of organic matter.<sup>37</sup> In a subsequent study, we saw the formation of both δ-MnO<sub>2</sub> and β-MnO<sub>2</sub> by O<sub>2</sub>\*- and ROO\* during nitrate photolysis in the presence of tert-butyl alcohol.<sup>38</sup> This finding indicated that organic matter indeed affected the mineral phases of Mn oxide solids. Note that these previous works tested Mn oxide formation in the solutions without any substrates (homogeneous nucleation). <sup>37, 38</sup> In contrast, the current study found that the heterogeneous nucleation and growth of Mn oxide solids on the nanoplastics induced the formation of mineral phases that were different from homogeneously formed Mn oxide solids. To further measure the Mn oxidation state of the formed Mn oxide solids on nanoplastics, X-ray photoelectron spectroscopy (XPS) was used. The XPS images in Figure 5b,c suggest that the MnO<sub>2</sub> solids formed by 30 and 100 nm PS-COOH nanoplastics contained mostly Mn(IV) (>98%) and little Mn(II) ( $\sim$ 1%), with no Mn(III), with an average oxidation state of  $\sim$ 3.97. More Mn(III) and Mn (II) were observed for Mn oxides formed by 100 nm PS-NH<sub>2</sub>, with a slightly lower average oxidation state of 3.84, as shown in Figure 5d. Note that in our previous study, 38 without

317

318

319

320

321

322

323

324

325

326

327

328

329

330

331

332

333

334

335

336

337

338

nanoplastics, homogeneously formed  $\delta$ -MnO<sub>2</sub> solids containing 73% Mn(IV) and 27% Mn(III) were generated. In Figure 2, Mn oxide solid concentrations were calculated assuming that Mn<sup>2+</sup>(aq) was oxidized to Mn(IV). Because the average oxidation state of Mn was slightly lower than 4 in the XPS result, the actual Mn oxide solids concentrations could be higher. Therefore, PS-based nanoplastics acting as substrates for heterogeneous nucleation of Mn oxide solids resulted in the formation of  $\alpha$ -MnO<sub>2</sub> as the main crystalline phase and changed the Mn oxidation state, which can influence the oxidation capability of Mn oxide solids.<sup>71</sup>

340

341

342

343

344

345

346

347

348

349

350

351

352

353

354

355

356

357

358

359

360

361

362

Impact of the Oxidative Capability of Nanoplastics on the Environment. As more plastic debris accumulates in the natural environment, there are increasing concerns about its adverse effects. These concerns are particularly acute for small nanoplastic particles that can more easily interact with neighboring substances, such as heavy metals and organic contaminants. This experimental work provides insights into the heterogeneous nucleation and growth of Mn oxide solids on such organic substrates, which benefits our understanding of Mn oxide occurrences in the environment. Mn oxide solids are excellent scavengers of redox-active species and heavy metals, further affecting geochemical element redox cycling, carbon mineralization, and biological metabolisms in nature.<sup>33-35</sup> Nanoplastics covered by MnO<sub>2</sub> solids might be co-transported in the above processes and interact with surrounding environmental compounds. In addition, the generation of ROS from nanoplastics can not only pose significant health risks to marine organisms by inducing the oxidation of tissues, 72 but also influence the mobility of nanoplastics in the environment via redox reactions. Furthermore, natural organic matter can interact with nanoplastics to form a "biofilm layer" which influences their stability and transportation, 73, 74 and may also affect their oxidative roles in the environment. Prolonged photoirradiation can age nanoplastics, altering their surface charge, roughness, and functional groups, and further affecting their oxidative capability.<sup>75</sup> Thus, the long-term effect of nanoplastic photolysis on the oxidation of transition and heavy metal ions deserves further systematic studies. Commercial nanoplastics were used in this study to investigate their oxidative role in Mn<sup>2+</sup> oxidation. The oxidative capability of additional environmental model nanoplastics<sup>76, 77</sup> merits future investigation.

### CONCLUSIONS

In summary, this study shows that nanoplastics not only had adsorption of metal ions but also facilitated redox reactions with heavy metals. This work revealed that photolysis of PS nanoplastics produced ROO\* and O2\*-, resulting in the fast oxidation of Mn²+(aq) to MnO2 solids. PS nanoplastics acted as active substrates and facilitated the heterogeneous nucleation and growth of Mn oxide solids. We also discovered that varying the particle sizes and functional groups of the PS nanoplastics affected the formation of Mn oxide solids, and that the coverage of Mn oxide solids on the surface of nanoplastics limited their further oxidative capability. These findings highlight the oxidative roles of nanoplastics in the formation of ROS and the oxidation of redoxactive metal ions in nature.

#### MATERIALS AND METHODS

Chemicals. All chemicals used in this study were at least American Chemical Society grade. Manganese chloride (MnCl<sub>2</sub>, 97%, anhydrous) was purchased from Beantown Chemical Co. (NH, USA). Leucoberbelin blue I (LBB, dye content 65%), potassium permanganate (KMnO<sub>4</sub>, ≥ 99%), superoxide dismutase bovine (SOD, ≥ 90%), polystyrene latex beads (PS, 100 nm mean particle size), carboxylate-modified polystyrene latex beads (PS-COOH, 30 or 500 nm mean particle size), and amine-modified polystyrene latex beads (PS-NH<sub>2</sub>, 100 nm mean particle size) were purchased from Millipore Sigma (MO, USA). Carboxylate-modified polystyrene latex beads (PS-COOH,

100 nm mean particle size) were purchased from Thermo Fisher Scientific (MO, USA). Sodium hydroxide (NaOH, > 97%), boric acid (H<sub>3</sub>BO<sub>3</sub>, > 99.5%), and *para*-aminobenzoic acid (PABA, > 90%) were bought from VWR International LLC. To prepare the solutions for all experiments, deionized (DI) water was used (resistivity  $\geq$  18.2 M $\Omega$ ·cm, Barnstead Ultrapure water systems). The stock solutions of 500 ppm nanoplastics were made by diluting the purchased standard solution with DI water and sonicating for 30 min. The stock solutions were then stored in brown bottles in the refrigerator at 4°C until use.

**Photo-oxidation Experiments.** Photolytic experiments were carried out in a 150 mL quartz reactor. Simulated solar light was provided by a 450 W Xenon arc lamp (Newport 6279NS) with an irradiance of 3.7 kW/m². The light was passed through flowing tap water, which filtered out near-infrared light and also cooled the reactor. For all experimental conditions, 0.1 mM MnCl₂ was the Mn source. The concentrations of dissolved Mn found in natural waters range from 10 to 10,000 μg/L (0.18 μM–0.18 mM).<sup>78-80</sup> Although the Mn concentrations used in this study may be higher than some of the values detected in natural surface waters, the findings can assist in better understanding a variety of geochemical conditions.

In this study, we chose to investigate a concentration of 10 ppm for PS-based nanoplastics, achieved by directly diluting the purchased nanoplastic chemicals (e.g., an aqueous suspension of 2.5% 100 nm PS-NH<sub>2</sub> solids) with DI water. The reported concentrations of microplastics in rivers and watersheds vary from ppb (μg/L) to several ppm.<sup>81-84</sup> Surface plastics concentrations have been statistically correlated with human population densities and urban development.<sup>83</sup> Because nanoplastics are extremely difficult to detect, only a few studies have reported their concentrations in real environmental samples. Nanoplastics were detected at the ppb level in Alpine snow samples.<sup>85</sup> In lab studies, the nanoplastics concentrations used mostly ranged from 1 to 100 ppm.<sup>86</sup>-

<sup>89</sup> In addition, here we chose pristine nanoplastics to investigate how the photolysis of nanoplastics affects Mn<sup>2+</sup> oxidation from a well-controlled starting point of experiment systems.

To understand the effects of pH on  $Mn^{2+}(aq)$  oxidation induced by photolysis of nanoplastics, solutions with and without borate buffer were studied for comparison. For experimental conditions without borate buffer, a solution containing 10 ppm of PS-COOH and 0.1 mM MnCl<sub>2</sub> was prepared. The solution's initial pH was adjusted to  $9.0 \pm 0.1$  by adding NaOH solution. This experimental pH is relevant to environmental systems, where the water quality guidelines for pH in freshwater set by the US Environmental Protection Agency (EPA) range from 6.5 to  $9.0.^{90}$  To facilitate experiments, we chose the high side of this pH range. For experimental conditions with borate buffer, a solution containing MnCl<sub>2</sub>, nanoplastics, and borate buffer was prepared. Borate buffer solutions, with a pKa of  $9.23.^{91}$  were made by adding NaOH to the boric acid solution to make 10 mM borate buffer at pH 9.

To examine the effects of nanoplastic size on Mn oxidation, solutions containing 0.1 mM MnCl<sub>2</sub>, 10 ppm of PS-COOH (30, 100, or 500 nm), and 10 mM borate buffer were prepared. The chosen sizes of PS-COOH span the range currently available from the chemical vendors Millipore Sigma and Thermo Fisher Scientific. To study the effect of surface chemical functional groups of nanoplastics on Mn oxidation, solutions containing 0.1 mM MnCl<sub>2</sub>, 10 ppm of 100 nm nanoplastic (PS-bare, PS-COOH, or PS-NH<sub>2</sub>), and 10 mM borate buffer were prepared. Because more ROS can be formed at a higher concentration of nanoplastics, we used the same concentrations of PS-based nanoplastics for comparison. The oxidation state of N in PS-NH<sub>2</sub> was identified by X-ray photoelectron spectroscopy (XPS, PHI 5000 VersaProbe II, UlvacPHI with monochromatic Al Kα radiation (1486.6 eV)). The C 1s peak (284.8 eV) was used as the reference peak. The chemical bonds of the dried PS-NH<sub>2</sub> and PS-bare nanoplastic samples were characterized with Fourier

transform infrared (FTIR) spectrometer (Thermo Scientific, Nicolet Nexus 470) equipped with a diamond crystal. The solution containing the same amount of nanoplastics was drop-casting on a Si wafer and then measured by FTIR after air drying. The FTIR spectra were plotted without any normalization of peak intensities, and thus can be semi-quantitatively compared.

Using a Xe arc lamp, the prepared solutions were exposed to simulated sunlight for 6 hours with continuous stirring. Samples were taken every hour to track the pH of the solution and the amounts of produced Mn oxide solids. The concentrations of Mn oxide solids formed under these conditions were measured for comparison by the LBB colorimetric method, which will explain in detail in the next section. The formed MnO<sub>2</sub> solid products were collected *via* centrifugation at 10,000 rpm for 30 min. The resulting solid products were then rinsed, resuspended in DI water, and centrifuged at 5,000 rpm for 5 minutes. The above process was repeated five times to eliminate impurities from the liquid supernatant. The solid products were dried at room temperature for further solid characterizations. In addition, Zetasizer Nano (Malvern Nano ZS) was used to measure the hydrodynamic diameter and zeta potential of nanoplastics in solutions under dark or photolysis conditions. At least duplicate experiments were conducted for each condition.

Quantification of Oxidized Mn Oxide Solids. Visual MINTEQ Version 3.1, a thermodynamic aqueous chemistry software, was used to calculate the saturation indices of representative Mn(II)/Mn(III)/Mn(IV) oxides at pH 9. Mn(OH)<sub>2</sub> solids would not form because the saturation index (SI) value of Mn(OH)<sub>2</sub> solids is -1.20 under the experimental conditions provided above. The SI values of common Mn(III)/Mn(IV) oxide minerals, such as birnessite (δ-MnO<sub>2</sub>), pyrolusite (β-MnO<sub>2</sub>), hausmannite (Mn<sub>3</sub>O<sub>4</sub>), and manganite (MnOOH) are 9.63, 11.69, 15.96, and 7.18, respectively. As a result, they can form under our test circumstances.

The concentrations of formed Mn(III)/Mn(IV) oxide solids in the experiments were quantified by the 0.004 % (w/v) LBB colorimetric method, as previously reported.<sup>37, 38</sup> Briefly, LBB was added to the taken samples and it then reduced Mn(III or IV) of the generated Mn oxide solids to Mn<sup>2+</sup>(aq). The UV-Vis intensity of the oxidized LBB compound at 625 nm was proportional to the concentration of oxidized Mn. To obtain a standard calibration curve for Mn oxide solids concentration calculation, LBB was added to different concentrations of KMnO<sub>4</sub> solutions to obtain a standard calibration curve for Mn oxide solids concentration versus UV-Vis absorbance at 625 nm (Figure S7).

453

454

455

456

457

458

459

460

461

462

463

464

465

466

467

468

469

470

471

472

473

474

475

Detection of Peroxyl and Superoxide Radicals Generated from the Photolysis of Nanoplastics. ROO was detected by a PABA fluorescent probe, as we previously reported. 38 This method utilizes the fact that PABA ( $\lambda_{ex} = 267$  nm, and  $\lambda_{em} = 334$  nm) loses its fluorescence when it is oxidized by ROO. 54 We performed the photolysis of a solution containing 20 mM PABA and 10 mM borate buffer as a control experiment because PABA is photodegraded during irradiation. Because PABA photodegradation is highly pH-dependent, <sup>56</sup> borate served as a buffer to stabilize the pH of the solution (pH = 9.0). To test the effects of simultaneous photodegradation and ROO. oxidation processes on PABA degradation, we conducted photolysis of a solution containing 20 μM PABA, 10 mM borate buffer, and 50 ppm PS-NH<sub>2</sub>. Our preliminary tests showed that, among PS-bare, PS-COOH, and PS-NH<sub>2</sub>, PS-NH<sub>2</sub> showed the clearest difference in PABA degradation in solutions with or without nanoplastics. So we focused on PS-NH<sub>2</sub> in this investigation. Here, PABA was degraded via irradiation and oxidization by ROO, which was produced from the photolysis of PS-NH<sub>2</sub>. To detect whether ROO was generated by photolysis of nanoplastics, the degradation of PABA was compared between the above two conditions. During the initial five minutes of the reaction, aqueous solution samples were taken every minute and immediately measured by a fluorometer (HORIBA Instruments Inc., Aqualog-UV-800-C). For each experimental condition, PABA concentrations were determined by individual calibration curves in the range from 2 to 20 μM PABA, where a linear relationship was observed between the concentrations and fluorescence intensities of PABA. An example of a calibration curve for a solution containing 10 mM borate buffer and PABA in a range from 2 to 20 μM is shown in Figure S8. To determine the corresponding oxidative role of O2<sup>+-</sup> generated from the photolysis of nanoplastics in Mn oxidation, SOD was added as an O2<sup>+-</sup> scavenger. Two solutions containing 0.1 mM MnCl<sub>2</sub>, 10 ppm of 30 nm PS-COOH, and 10 mM borate buffer, one with and the other without 0.5 μM SOD, were prepared for the comparison of Mn oxidation. The solution pH values at selected time points were also measured. At least duplicate experiments were conducted for each condition.

Mn Oxides Solid Phase Characterization. To identify the mineral phase of Mn oxide solids, high-resolution X-ray diffraction (HRXRD, Bruker D8 Advance X-ray diffractometer with Cu K $\alpha$  radiation ( $\lambda$  = 1.5418 Å)) was utilized. Mn oxidation states in the Mn oxide solid samples were identified by XPS. To determine the ratio of Mn(II), Mn(III), and Mn(IV), the Mn 2p<sub>3/2</sub> spin orbit was fitted with Mn(II) (640.8eV), Mn(III) (641.8 eV), and Mn(IV) (642.2 eV) by the Gauss-Lorentz fitting method, based on previously reported values of the Mn 2p<sub>3/2</sub> spectrum. High-resolution transmission electron microscopy (HR-TEM, JEOL-2100F field emission) was utilized to image the morphologies and to conduct element mapping of nanoplastics and formed Mn oxide solids. After 6 hr of photochemical reaction, approximately 50  $\mu$ L of the solution was placed on an ultrathin lacey carbon film coated-Cu grid (LC400-Cu-CC-25, Electron Microscopy Science, PA) for imaging. Electron diffraction patterns for selected areas were obtained to determine the phases of Mn oxide solids.

#### ASSOCIATED CONTENT

#### **Supporting Information Available**

No Mn oxidation is observed under the dark condition in Figure S1a. Figure S1b shows the control experiments of Mn oxidation by borate and by surfactant in the purchased chemical. STEM images of Mn oxide solids on 30 nm PS-COOH are shown in Figure S2. Figure S3 shows the FTIR spectra of PS-bare nanoplastics dried on a Si wafer. Figure S4 shows the pH change under the conditions of 20 μM PABA and 10 mM borate buffer with/without 50 ppm of 100 nm PS-NH; and 0.1 mM MnCl<sub>2</sub>, 10 ppm of 30 nm PS-COOH, and 10 mM borate buffer with/without 0.5 μM SOD. Figure S5 shows the individual contributions to Mn oxidation by ROO\* and O2\* generated from the different particle sizes of PS-COOH and PS with other functional groups (PS-NH<sub>2</sub> and PS-bare). Hydrodynamic diameters and zeta potential values of nanoplastics during the reaction are in Figure S6. Figure S7 is a calibration curve for determining the concentration of Mn(IV)O2. Figure S8 is an example calibration curve for a solution containing 10 mM borate buffer and PABA in the range from 2 to 20 μM. Table S1 summarizes XPS references for Mn(II), Mn(III), and Mn(IV).

#### **Conflict of Interest**

The authors declare that they have no known competing financial interests or personal relationships that could have appeared to influence the work reported in this paper.

#### ACKNOWLEDGMENTS

The authors are grateful for the support received from the National Science Foundation's Environmental Chemical Sciences program (CHE-1905077). P.-I. Chou acknowledges the fellowship from the McDonnell International Scholars Academy. The authors would like to acknowledge the Nano Research Facility (NRF) of Washington University in St. Louis for use of

the fluorometer and the Institute of Materials Science & Engineering (IMSE) for the use of XPS and TEM. The authors thank the members of the Environmental NanoChemistry Group for valuable discussions, and Professor James C. Ballard for carefully reviewing the manuscript.

#### 524 • REFERENCES

- 525 (1) Andrady, A. L.; Neal, M. A. Applications and Societal Benefits of Plastics. *Philosophical*
- 526 Transactions of the Royal Society B: Biological Sciences 2009, 364 (1526), 1977-1984.
- 527 (2) Geyer, R. Production, Use, and Fate of Synthetic Polymers. In *Plastic Waste and Recycling*,
- 528 Letcher, T. M. Ed.; Academic Press, 2020; pp 13-32.
- 529 (3) Geyer, R.; Jambeck, J. R.; Law, K. L. Production, Use, and Fate of All Plastics Ever Made.
- 530 *Science advances* **2017**, *3* (7), e1700782.
- 531 (4) Andrady, A. L. Microplastics in the Marine Environment. Mar. Pollut. Bull. 2011, 62 (8), 1596-
- 532 1605.
- 533 (5) Chamas, A.; Moon, H.; Zheng, J.; Qiu, Y.; Tabassum, T.; Jang, J. H.; Abu-Omar, M.; Scott, S.
- L.; Suh, S. Degradation Rates of Plastics in the Environment. ACS Sustainable Chem. Eng. 2020,
- 535 8 (9), 3494-3511.
- 536 (6) Wang, X.; Zheng, H.; Zhao, J.; Luo, X.; Wang, Z.; Xing, B. Photodegradation Elevated the
- Toxicity of Polystyrene Microplastics to Grouper (Epinephelus Moara) through Disrupting
- 538 Hepatic Lipid Homeostasis. *Environ. Sci. Technol.* **2020**, *54* (10), 6202-6212.
- 539 (7) Alimi, O. S.; Farner Budarz, J.; Hernandez, L. M.; Tufenkji, N. Microplastics and Nanoplastics
- 540 in Aquatic Environments: Aggregation, Deposition, and Enhanced Contaminant Transport.
- 541 Environ. Sci. Technol. 2018, 52 (4), 1704-1724.
- 542 (8) Lambert, S.; Wagner, M. Characterisation of Nanoplastics during the Degradation of
- 543 Polystyrene. *Chemosphere* **2016**, *145*, 265-268.
- 544 (9) Artham, T.; Doble, M. Biodegradation of Aliphatic and Aromatic Polycarbonates. *Macromol.*
- 545 *Biosci.* **2008**, 8 (1), 14-24.
- 546 (10) Law, K. L.; Thompson, R. C. Microplastics in the Seas. *Science* **2014**, *345* (6193), 144-145.
- 547 (11) Moore, C. J. Synthetic Polymers in the Marine Environment: A Rapidly Increasing, Long-
- 548 Term Threat. *Environ. Res.* **2008**, *108* (2), 131-139.
- 549 (12) Ter Halle, A.; Ghiglione, J. F. Nanoplastics: A Complex, Polluting Terra Incognita. *Environ*.
- 550 Sci. Technol. **2021**, 55 (21), 14466-14469.
- 551 (13) Gigault, J.; Ter Halle, A.; Baudrimont, M.; Pascal, P.-Y.; Gauffre, F.; Phi, T.-L.; El Hadri, H.;
- Grassl, B.; Reynaud, S. Current Opinion: What Is a Nanoplastic? *Environ. Pollut.* **2018**, *235*, 1030-
- 553 1034.
- 554 (14) Gall, S. C.; Thompson, R. C. The Impact of Debris on Marine Life. Mar. Pollut. Bull. 2015,
- 555 *92* (1-2), 170-179.
- 556 (15) Gregory, M. R. Environmental Implications of Plastic Debris in Marine Settings—
- 557 Entanglement, Ingestion, Smothering, Hangers-on, Hitch-Hiking and Alien Invasions.
- Philosophical Transactions of the Royal Society B: Biological Sciences 2009, 364 (1526), 2013-
- 559 2025.
- 560 (16) Cole, M.; Lindeque, P.; Fileman, E.; Halsband, C.; Goodhead, R.; Moger, J.; Galloway, T. S.
- Microplastic Ingestion by Zooplankton. Environ. Sci. Technol. 2013, 47 (12), 6646-6655.

- 562 (17) Tallec, K.; Blard, O.; González-Fernández, C.; Brotons, G.; Berchel, M.; Soudant, P.; Huvet,
- A.; Paul-Pont, I. Surface Functionalization Determines Behavior of Nanoplastic Solutions in
- Model Aquatic Environments. *Chemosphere* **2019**, *225*, 639-646.
- 565 (18) Holmes, L. A.; Turner, A.; Thompson, R. C. Adsorption of Trace Metals to Plastic Resin
- Pellets in the Marine Environment. *Environ. Pollut.* **2012**, *160*, 42-48.
- 567 (19) Tang, S.; Lin, L.; Wang, X.; Yu, A.; Sun, X. Interfacial Interactions between Collected Nylon
- Microplastics and Three Divalent Metal Ions (Cu(II), Ni(II), Zn(II)) in Aqueous Solutions. J.
- 569 *Hazard. Mater.* **2021**, *403*, 123548.
- 570 (20) Turner, A.; Holmes, L. A. Adsorption of Trace Metals by Microplastic Pellets in Fresh Water.
- 571 Environmental chemistry **2015**, 12 (5), 600-610.
- 572 (21) Dong, Y.; Gao, M.; Song, Z.; Qiu, W. As(III) Adsorption onto Different-Sized Polystyrene
- 573 Microplastic Particles and Its Mechanism. *Chemosphere* **2020**, *239*, 124792.
- 574 (22) Pascall, M. A.; Zabik, M. E.; Zabik, M. J.; Hernandez, R. J. Uptake of Polychlorinated
- 575 Biphenyls (PCBs) from an Aqueous Medium by Polyethylene, Polyvinyl Chloride, and
- 576 Polystyrene Films. *J. Agric. Food. Chem.* **2005**, *53* (1), 164-169.
- 577 (23) Lee, H.; Shim, W. J.; Kwon, J.-H. Sorption Capacity of Plastic Debris for Hydrophobic
- 578 Organic Chemicals. Sci. Total Environ. 2014, 470, 1545-1552.
- 579 (24) Rochman, C. M.; Hoh, E.; Hentschel, B. T.; Kaye, S. Long-Term Field Measurement of
- Sorption of Organic Contaminants to Five Types of Plastic Pellets: Implications for Plastic Marine
- 581 Debris. Environ. Sci. Technol. 2013, 47 (3), 1646-1654.
- 582 (25) Mato, Y.; Isobe, T.; Takada, H.; Kanehiro, H.; Ohtake, C.; Kaminuma, T. Plastic Resin Pellets
- as a Transport Medium for Toxic Chemicals in the Marine Environment. *Environ. Sci. Technol.*
- **2001**, *35* (2), 318-324.
- 585 (26) Van, A.; Rochman, C. M.; Flores, E. M.; Hill, K. L.; Vargas, E.; Vargas, S. A.; Hoh, E.
- Persistent Organic Pollutants in Plastic Marine Debris Found on Beaches in San Diego, California.
- 587 *Chemosphere* **2012**, *86* (3), 258-263.
- 588 (27) Zhu, K.; Jia, H.; Zhao, S.; Xia, T.; Guo, X.; Wang, T.; Zhu, L. Formation of Environmentally
- Persistent Free Radicals on Microplastics under Light Irradiation. Environ. Sci. Technol. 2019, 53
- 590 (14), 8177-8186.
- 591 (28) Zhu, K.; Jia, H.; Sun, Y.; Dai, Y.; Zhang, C.; Guo, X.; Wang, T.; Zhu, L. Long-Term
- 592 Phototransformation of Microplastics under Simulated Sunlight Irradiation in Aquatic
- Environments: Roles of Reactive Oxygen Species. Water Res. 2020, 173, 115564.
- 594 (29) Suhrhoff, T. J.; Scholz-Böttcher, B. M. Qualitative Impact of Salinity, UV Radiation and
- 595 Turbulence on Leaching of Organic Plastic Additives from Four Common Plastics—A Lab
- 596 Experiment. Mar. Pollut. Bull. 2016, 102 (1), 84-94.
- 597 (30) Gewert, B.; Plassmann, M.; Sandblom, O.; MacLeod, M. Identification of Chain Scission
- 598 Products Released to Water by Plastic Exposed to Ultraviolet Light. Environmental Science &
- 599 *Technology Letters* **2018**, *5* (5), 272-276.

- 600 (31) Wang, X.; Li, Y.; Zhao, J.; Xia, X.; Shi, X.; Duan, J.; Zhang, W. UV-Induced Aggregation of
- 601 Polystyrene Nanoplastics: Effects of Radicals, Surface Functional Groups and Electrolyte.
- 602 Environmental Science: Nano **2020**, 7 (12), 3914-3926.
- 603 (32) Tian, L.; Chen, Q.; Jiang, W.; Wang, L.; Xie, H.; Kalogerakis, N.; Ma, Y.; Ji, R. A Carbon-
- 604 14 Radiotracer-Based Study on the Phototransformation of Polystyrene Nanoplastics in Water
- 605 *versus* in Air. *Environmental Science: Nano* **2019**, *6* (9), 2907-2917.
- 606 (33) Myers, C. R.; Nealson, K. H. Bacterial Manganese Reduction and Growth with Manganese
- Oxide as the Sole Electron Acceptor. *Science* **1988**, *240* (4857), 1319-1321.
- 608 (34) Tebo, B. M.; Bargar, J. R.; Clement, B. G.; Dick, G. J.; Murray, K. J.; Parker, D.; Verity, R.;
- Webb, S. M. Biogenic Manganese Oxides: Properties and Mechanisms of Formation. Annu. Rev.
- 610 Earth Planet. Sci. **2004**, 32, 287-328.
- 611 (35) Butterfield, C. N.; Soldatova, A. V.; Lee, S.-W.; Spiro, T. G.; Tebo, B. M. Mn(II, III)
- Oxidation and MnO<sub>2</sub> Mineralization by an Expressed Bacterial Multicopper Oxidase. *Proc. Natl.*
- 613 Acad. Sci. U. S. A. **2013**, 110 (29), 11731-11735.
- 614 (36) Catrouillet, C.; Davranche, M.; Khatib, I.; Fauny, C.; Wahl, A.; Gigault, J. Metals in
- Microplastics: Determining Which Are Additive, Adsorbed, and Bioavailable. Env. Sci. Process.
- 616 *Impact.* **2021**, *23* (4), 553-558.
- 617 (37) Jung, H.; Chadha, T. S.; Kim, D.; Biswas, P.; Jun, Y.-S. Photochemically Assisted Fast
- 618 Abiotic Oxidation of Manganese and Formation of δ-MnO<sub>2</sub> Nanosheets in Nitrate Solution. *Chem.*
- 619 *Commun.* **2017**, *53* (32), 4445-4448.
- 620 (38) Gao, Z.; Zhang, D.; Jun, Y.-S. Does Tert-Butyl Alcohol Really Terminate the Oxidative
- Activity of OH in Inorganic Redox Chemistry? *Environ. Sci. Technol.* **2021**, *55* (15), 10442-10450.
- 622 (39) Learman, D.; Voelker, B.; Vazquez-Rodriguez, A.; Hansel, C. Formation of Manganese
- Oxides by Bacterially Generated Superoxide. *Nat. Geosci.* **2011**, 4 (2), 95-98.
- 624 (40) Hansel, C. M.; Francis, C. A. Coupled Photochemical and Enzymatic Mn(II) Oxidation
- Pathways of a Planktonic Roseobacter-Like Bacterium. Appl. Environ. Microbiol. 2006, 72 (5),
- 626 3543-3549.
- 627 (41) Learman, D.; Wankel, S.; Webb, S.; Martinez, N.; Madden, A.; Hansel, C. Coupled Biotic-
- 628 Abiotic Mn(II) Oxidation Pathway Mediates the Formation and Structural Evolution of Biogenic
- 629 Mn Oxides. Geochim. Cosmochim. Acta 2011, 75 (20), 6048-6063.
- 630 (42) Diaz, J. M.; Hansel, C. M.; Voelker, B. M.; Mendes, C. M.; Andeer, P. F.; Zhang, T.
- Widespread Production of Extracellular Superoxide by Heterotrophic Bacteria. Science 2013,
- 632 1237331.
- 633 (43) Hansel, C. M.; Zeiner, C. A.; Santelli, C. M.; Webb, S. M. Mn(II) Oxidation by an
- Ascomycete Fungus Is Linked to Superoxide Production During Asexual Reproduction. *Proc. Natl.*
- 635 Acad. Sci. U. S. A. **2012**, 109 (31), 12621-12625.
- 636 (44) Gao, Z.; Liu, J.; Skurie, C.; Zhu, Y.; Jun, Y.-S. Photochemical Reactions of Dissolved Organic
- Matter and Bromide Ions Facilitate Abiotic Formation of Manganese Oxide Solids. *Water Res.*
- 638 **2022**, *222*, 118831.

- 639 (45) Crawford, K. D.; Hughes, K. D. Rapid Formation and Spectroscopic Observation of
- Polystyrene Conjugation in Individual Micron-Diameter Particles with Visible Radiation. J. Phys.
- 641 *Chem. B* **1997**, *101* (6), 864-870.
- 642 (46) Kuzina, S.; Mikhailov, A. Photo-Oxidation of Polymers—2. Photo-Chain Reaction of
- 643 Peroxide Radicals in Polystyrene. *Eur. Polym. J.* **1998**, *34* (2), 291-299.
- 644 (47) Kerr, J. Bond Dissociation Energies by Kinetic Methods. Chem. Rev. 1966, 66 (5), 465-500.
- 645 (48) Benson, S. W. III-Bond Energies. J. Chem. Educ. 1965, 42 (9), 502.
- 646 (49) Christensen, H.; Sehested, K.; Corfitzen, H. Reactions of Hydroxyl Radicals with Hydrogen
- Peroxide at Ambient and Elevated Temperatures. J. Phys. Chem. 1982, 86 (9), 1588-1590.
- 648 (50) Geuskens, G.; Baeyens-Volant, D.; Delaunois, G.; Lu-Vinh, Q.; Piret, W.; David, C. Photo-
- Oxidation of Polymers—I: A Quantitative Study of the Chemical Reactions Resulting from
- 650 Irradiation of Polystyrene at 253.7 nm in the Presence of Oxygen. Eur. Polym. J. 1978, 14 (4),
- 651 291-297.
- 652 (51) Bracco, P.; Costa, L.; Luda, M. P.; Billingham, N. A Review of Experimental Studies of the
- Role of Free-Radicals in Polyethylene Oxidation. *Polym. Degrad. Stab.* **2018**, *155*, 67-83.
- 654 (52) Rocha, M.; Mansur, A.; Mansur, H. Characterization and Accelerated Ageing of Uhmwpe
- Used in Orthopedic Prosthesis by Peroxide. *Materials* **2009**, *2* (2), 562-576.
- 656 (53) Bracco, P.; Brunella, V.; Zanetti, M.; Luda, M.; Costa, L. Stabilisation of Ultra-High
- Molecular Weight Polyethylene with Vitamin E. Polym. Degrad. Stab. 2007, 92 (12), 2155-2162.
- 658 (54) Guclu, K.; Kıbrıslıoğlu, G. l. a.; Ozyurek, M.; Apak, R. Development of a Fluorescent Probe
- 659 for Measurement of Peroxyl Radical Scavenging Activity in Biological Samples. J. Agric. Food.
- 660 *Chem.* **2014**, *62* (8), 1839-1845.
- 661 (55) Krumova, K.; Cosa, G. Overview of Reactive Oxygen Species. In Singlet Oxygen:
- Applications in Biosciences and Nanosciences, Vol. 1; The Royal Society of Chemistry, 2016; pp
- 663 1-21.
- 664 (56) Zhou, L.; Ji, Y.; Zeng, C.; Zhang, Y.; Wang, Z.; Yang, X. Aquatic Photodegradation of
- Sunscreen Agent p-Aminobenzoic Acid in the Presence of Dissolved Organic Matter. Water Res.
- 666 **2013**, *47* (1), 153-162.
- 667 (57) Gao, Z.; Skurie, C.; Jun, Y.-S. Reactive Halogen Radicals in Saline Water Promote
- Photochemically-Assisted Formation of Manganese Oxide Nanosheets. *Environmental Science*:
- 669 Nano **2022**, 9 (10), 3756-3765.
- 670 (58) Godwin, C. M.; Zehnpfennig, J. R.; Learman, D. R. Biotic and Abiotic Mechanisms of
- Manganese(II) Oxidation in Lake Erie. Frontiers in Environmental Science 2020, 8, 57.
- 672 (59) Nico, P. S.; Anastasio, C.; Zasoski, R. J. Rapid Photo-Oxidation of Mn(II) Mediated by Humic
- 673 Substances. *Geochim. Cosmochim. Acta* **2002**, *66* (23), 4047-4056.
- 674 (60) Learman, D. R.; Voelker, B. M.; Madden, A. S.; Hansel, C. M. Constraints on Superoxide
- Mediated Formation of Manganese Oxides. Front. Microbiol. 2013, 4, 262.
- 676 (61) Im, J. K.; Son, H. S.; Kang, Y. M.; Zoh, K. D. Carbamazepine Degradation by Photolysis and
- Titanium Dioxide Photocatalysis. Water Environ. Res 2012, 84 (7), 554-561.

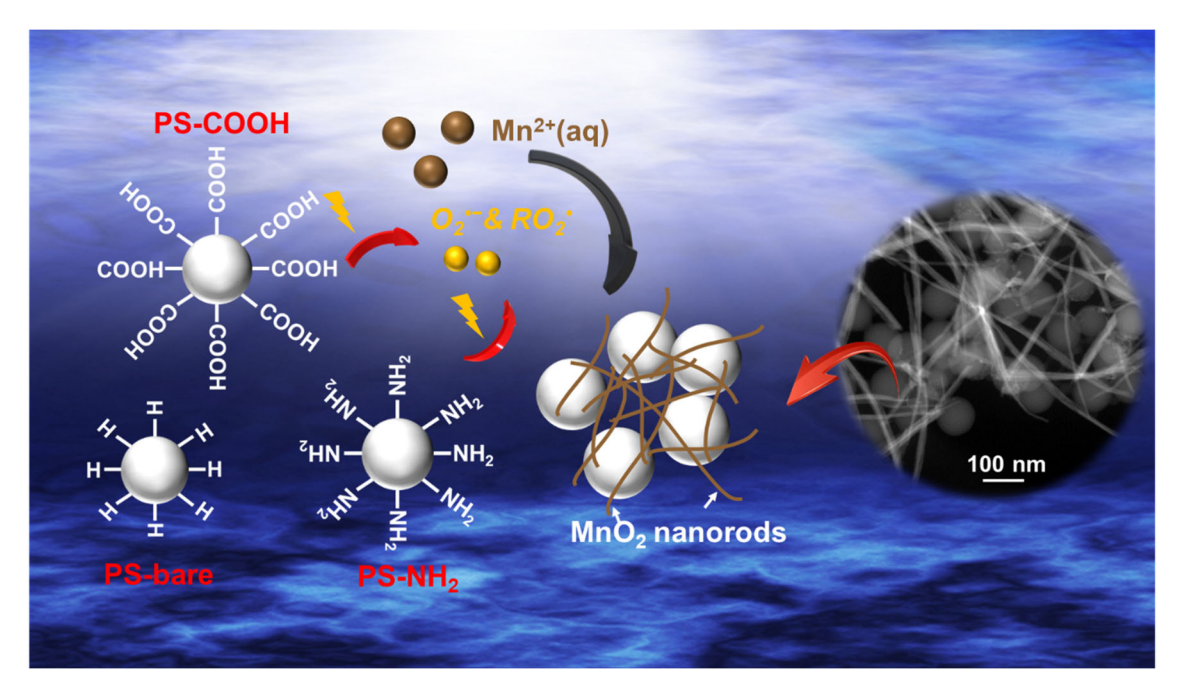
- 678 (62) Yang, W.; You, D.; Li, C.; Han, C.; Tang, N.; Yang, H.; Xue, X. Photolysis of Nitroaromatic
- 679 Compounds under Sunlight: A Possible Daytime Photochemical Source of Nitrous Acid?
- 680 Environmental Science & Technology Letters 2021, 8 (9), 747-752.
- 681 (63) Mack, J.; Bolton, J. R. Photochemistry of Nitrite and Nitrate in Aqueous Solution: A Review.
- 682 J. Photochem. Photobiol. A: Chem. 1999, 128 (1-3), 1-13.
- 683 (64) Wach, R. A.; Kudoh, H.; Zhai, M.; Muroya, Y.; Katsumura, Y. Laser Flash Photolysis of
- 684 Carboxymethylcellulose in an Aqueous Solution. J. Polym. Sci., Part A: Polym. Chem. 2005, 43
- 685 (3), 505-518.
- 686 (65) Rhydderch, S.; Howe, R. F. In Situ EPR Studies of Reaction Pathways in Titania
- Photocatalyst-Promoted Alkylation of Alkenes. *Molecules* **2015**, *20* (3), 4055-4070.
- 688 (66) Schuchmann, M. N.; Von Sonntag, C. Hydroxyl Radical-Induced Oxidation of 2-Methyl-2-
- Propanol in Oxygenated Aqueous Solution. A Product and Pulse Radiolysis Study. J. Phys. Chem.
- 690 **1979**, *83* (7), 780-784.
- 691 (67) Von Sonntag, C.; Von Gunten, U. Reactions of Hydroxyl and Peroxyl Radicals. In *Chemistry*
- 692 of Ozone in Water and Wastewater Treatment, IWA publishing, 2012; pp 225-248.
- 693 (68) Schulte-Frohlinde, D.; Behrens, G.; Önal, A. Lifetime of Peroxyl Radicals of Poly (U), Poly
- 694 (A) and Single-and Double-Stranded DNA and the Rate of Their Reaction with Thiols. Int. J.
- 695 Radiat. Biol. Relat. Stud. Phys. Chem. Med. 1986, 50 (1), 103-110.
- 696 (69) Levy, M.; Chowdhury, P. P.; Nagpal, P. Quantum Dot Therapeutics: A New Class of Radical
- 697 Therapies. J. Biol. Eng. 2019, 13 (1), 1-12.
- 698 (70) Pecora, R. Dynamic Light Scattering Measurement of Nanometer Particles in Liquids. J.
- 699 Nanopart. Res. **2000**, 2 (2), 123-131.
- 700 (71) Hayashi, E.; Yamaguchi, Y.; Kamata, K.; Tsunoda, N.; Kumagai, Y.; Oba, F.; Hara, M. Effect
- 701 of MnO<sub>2</sub> Crystal Structure on Aerobic Oxidation of 5-Hydroxymethylfurfural to 2, 5-
- 702 Furandicarboxylic Acid. J. Am. Chem. Soc. **2019**, 141 (2), 890-900.
- 703 (72) Hu, M.; Palić, D. Micro-and Nano-Plastics Activation of Oxidative and Inflammatory
- Adverse Outcome Pathways. *Redox Biology* **2020**, 101620.
- 705 (73) Ali, I.; Tan, X.; Li, J.; Peng, C.; Naz, I.; Duan, Z.; Ruan, Y. Interaction of Microplastics and
- Nanoplastics with Natural Organic Matter (NOM) and the Impact of NOM on the Sorption
- 707 Behavior of Anthropogenic Contaminants-A Critical Review. Journal of Cleaner Production
- 708 **2022**, 134314.
- 709 (74) Fadare, O. O.; Wan, B.; Liu, K.; Yang, Y.; Zhao, L.; Guo, L.-H. Eco-Corona vs Protein
- 710 Corona: Effects of Humic Substances on Corona Formation and Nanoplastic Particle Toxicity in
- 711 Daphnia Magna. Environ. Sci. Technol. **2020**, *54* (13), 8001-8009.
- 712 (75) Shen, M.; Zhang, Y.; Zhu, Y.; Song, B.; Zeng, G.; Hu, D.; Wen, X.; Ren, X. Recent Advances
- 713 in Toxicological Research of Nanoplastics in the Environment: A Review. *Environ. Pollut.* **2019**,
- 714 *252*, 511-521.
- 715 (76) El Hadri, H.; Gigault, J.; Maxit, B.; Grassl, B.; Reynaud, S. Nanoplastic from Mechanically
- 716 Degraded Primary and Secondary Microplastics for Environmental Assessments. NanoImpact
- 717 **2020**, *17*, 100206.

- 718 (77) Blancho, F.; Davranche, M.; Fumagalli, F.; Ceccone, G.; Gigault, J. A Reliable Procedure to
- 719 Obtain Environmentally Relevant Nanoplastic Proxies. *Environmental Science: Nano* **2021**, 8 (11),
- 720 3211-3219.
- 721 (78) WHO. Concise International Chemical Assessment Document 12, Manganese and Its
- 722 Compounds; World Health Organization, 1999.
- 723 <a href="https://inchem.org/documents/cicads/cicads/cicad12.htm">https://inchem.org/documents/cicads/cicads/cicad12.htm</a>.
- 724 (79) WHO. Concise International Chemical Assessment Document 63, Manganese and Its
- 725 Compounds: Environmental Aspects; World Health Organization, 2004.
- 726 https://inchem.org/documents/cicads/cicads/cicad63.htm.
- 727 (80) Williams, M.; Todd, G. D.; Roney, N.; Crawford, J.; Coles, C.; McClure, P. R.; Garey, J. D.;
- 728 Zaccaria, K.; Citra, M. Toxicological Profile for Manganese; Agency for Toxic Substances and
- 729 Disease Registry: Atlanta, USA, 2013.
- 730 (81) Lebreton, L. C.; Van Der Zwet, J.; Damsteeg, J.-W.; Slat, B.; Andrady, A.; Reisser, J. River
- Plastic Emissions to the World's Oceans. *Nat. Commun.* **2017**, 8 (1), 1-10.
- 732 (82) Lechner, A.; Keckeis, H.; Lumesberger-Loisl, F.; Zens, B.; Krusch, R.; Tritthart, M.; Glas,
- 733 M.; Schludermann, E. The Danube So Colourful: A Potpourri of Plastic Litter Outnumbers Fish
- Tavae in Europe's Second Largest River. Environ. Pollut. 2014, 188, 177-181.
- 735 (83) Yonkos, L. T.; Friedel, E. A.; Perez-Reyes, A. C.; Ghosal, S.; Arthur, C. D. Microplastics in
- Four Estuarine Rivers in the Chesapeake Bay, USA. Environ. Sci. Technol. 2014, 48 (24), 14195-
- 737 14202.
- 738 (84) Zhao, S.; Zhu, L.; Wang, T.; Li, D. Suspended Microplastics in the Surface Water of the
- Yangtze Estuary System, China: First Observations on Occurrence, Distribution. Mar. Pollut. Bull.
- 740 **2014**, *86* (1-2), 562-568.
- 741 (85) Materić, D. a.; Kasper-Giebl, A.; Kau, D.; Anten, M.; Greilinger, M.; Ludewig, E.; van Sebille,
- 742 E.; Röckmann, T.; Holzinger, R. Micro-and Nanoplastics in Alpine Snow: A New Method for
- 743 Chemical Identification and (Semi) Quantification in the Nanogram Range. *Environ. Sci. Technol.*
- 744 **2020**, *54* (4), 2353-2359.
- 745 (86) Besseling, E.; Quik, J. T.; Sun, M.; Koelmans, A. A. Fate of Nano-and Microplastic in
- 746 Freshwater Systems: A Modeling Study. *Environ. Pollut.* **2017**, *220*, 540-548.
- 747 (87) Zhuang, J.; Qi, J.; Jin, Y. Retention and Transport of Amphiphilic Colloids under Unsaturated
- 748 Flow Conditions: Effect of Particle Size and Surface Property. Environ. Sci. Technol. 2005, 39
- 749 (20), 7853-7859.
- 750 (88) Mitzel, M. R.; Sand, S.; Whalen, J. K.; Tufenkji, N. Hydrophobicity of Biofilm Coatings
- 751 Influences the Transport Dynamics of Polystyrene Nanoparticles in Biofilm-Coated Sand. Water
- 752 Res. **2016**, 92, 113-120.
- 753 (89) Xu, S.; Qi, J.; Chen, X.; Lazouskaya, V.; Zhuang, J.; Jin, Y. Coupled Effect of Extended
- 754 DLVO and Capillary Interactions on the Retention and Transport of Colloids through Unsaturated
- 755 Porous Media. Sci. Total Environ. 2016, 573, 564-572.
- 756 (90) EPA. Ground Water and Drinking Water. Environmental Protection Agency, 2022.
- 757 https://www.epa.gov/ground-water-and-drinking-water/basic-information-about-lead-drinking-
- water (accessed 2022 October 7).

- 759 (91) Stoll, V. S.; Blanchard, J. S. Buffers: Principles and Practice. Methods Enzymol. 2009, 463,
- 760 43-56.

- 761 (92) Jung, H.; Chadha, T. S.; Min, Y.; Biswas, P.; Jun, Y.-S. Photochemically-Assisted Synthesis
- of Birnessite Nanosheets and Their Structural Alteration in the Presence of Pyrophosphate. ACS
- 763 Sustainable Chem. Eng. **2017**, 5 (11), 10624-10632.

# **TOC Art**



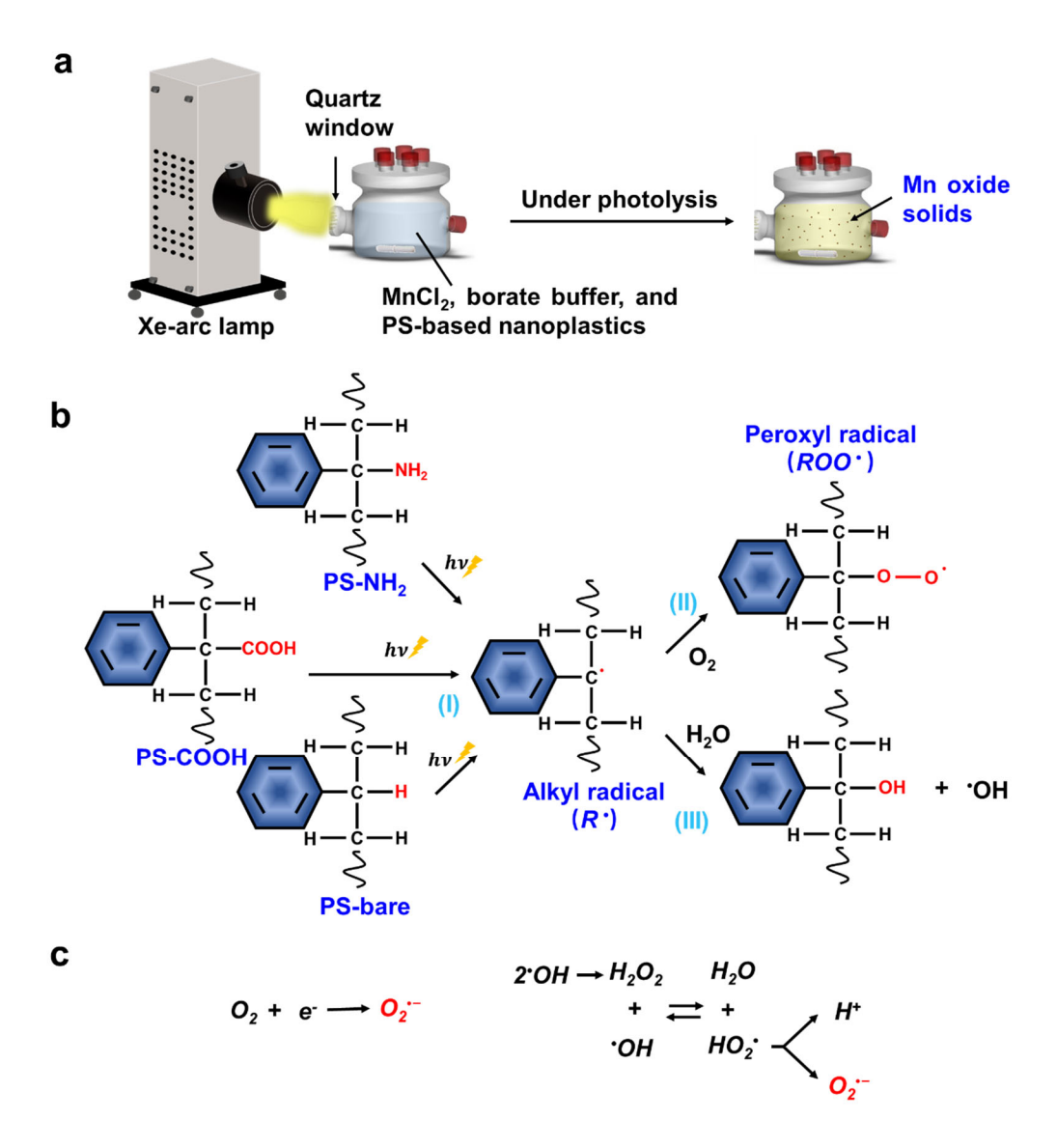


**Figure 1.** (a) Schematic illustration of the photolytic experiment of Mn oxide solids formation in the presence of PS-based nanoplastics. (b and c) Pathways for generating reactive oxygen species (ROS) during photolysis of nanoplastics. Proposed pathways for the generation of (b) ROO\* and (c) O2\*.

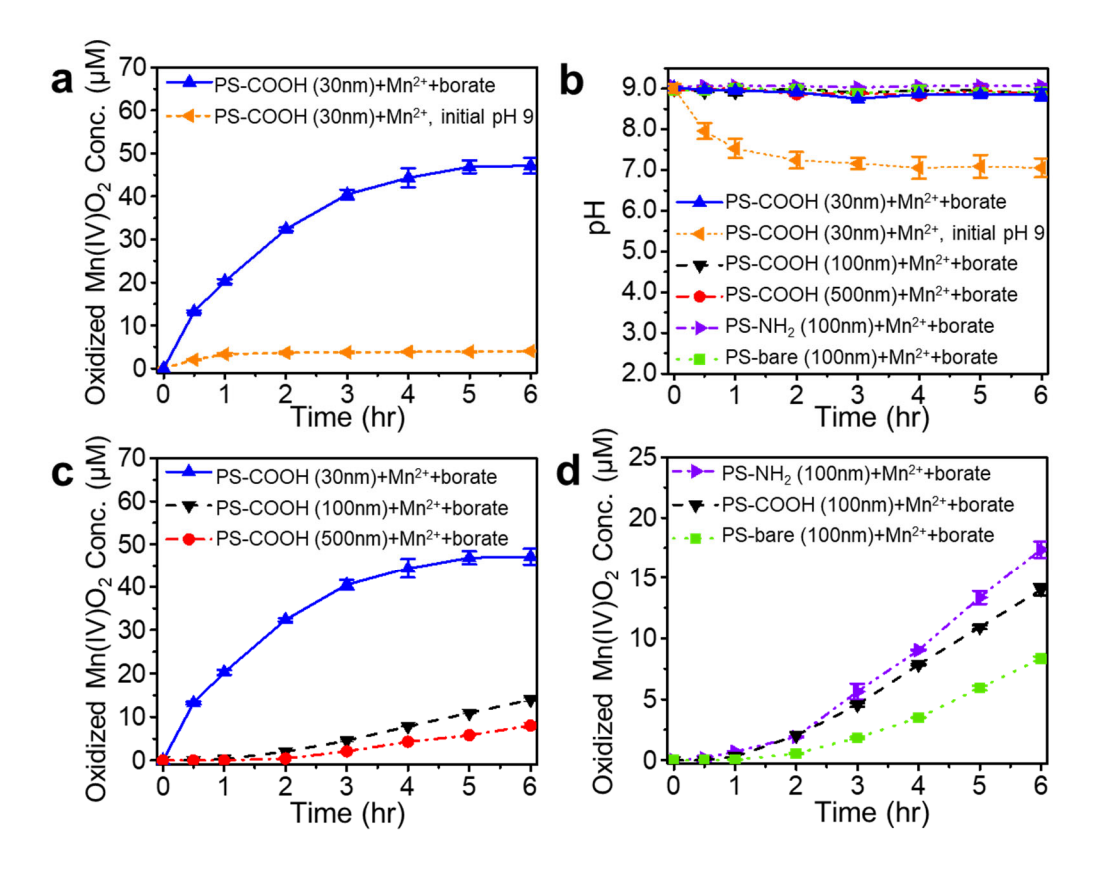


Figure 2. Effects of pH, particle sizes, and functional groups of nanoplastics on Mn oxidation. (a) Oxidized Mn concentrations with elapsed experimental time under the conditions of 0.1 mM MnCl<sub>2</sub>, 10 ppm of 30 nm PS-COOH, with/without 10 mM borate buffer at initial pH 9. (b) Solution pH with elapsed experimental time in (a), (c), and (d). (c) Oxidized Mn concentrations on different sizes of PS-COOH nanoparticles with elapsed experimental time under the conditions of 0.1 mM MnCl<sub>2</sub>, 10 ppm of PS-COOH (30, 100, or 500 nm), and 10 mM borate buffer. (d) Oxidized Mn concentrations on different functional groups of PS-based nanoplastics with elapsed experimental time under the conditions of 0.1 mM MnCl<sub>2</sub>, 10 ppm of 100 nm PS-NH<sub>2</sub>, PS-COOH, or PS-bare, and 10 mM borate buffer. Error bars represent the standard deviation from at least duplicate tests.

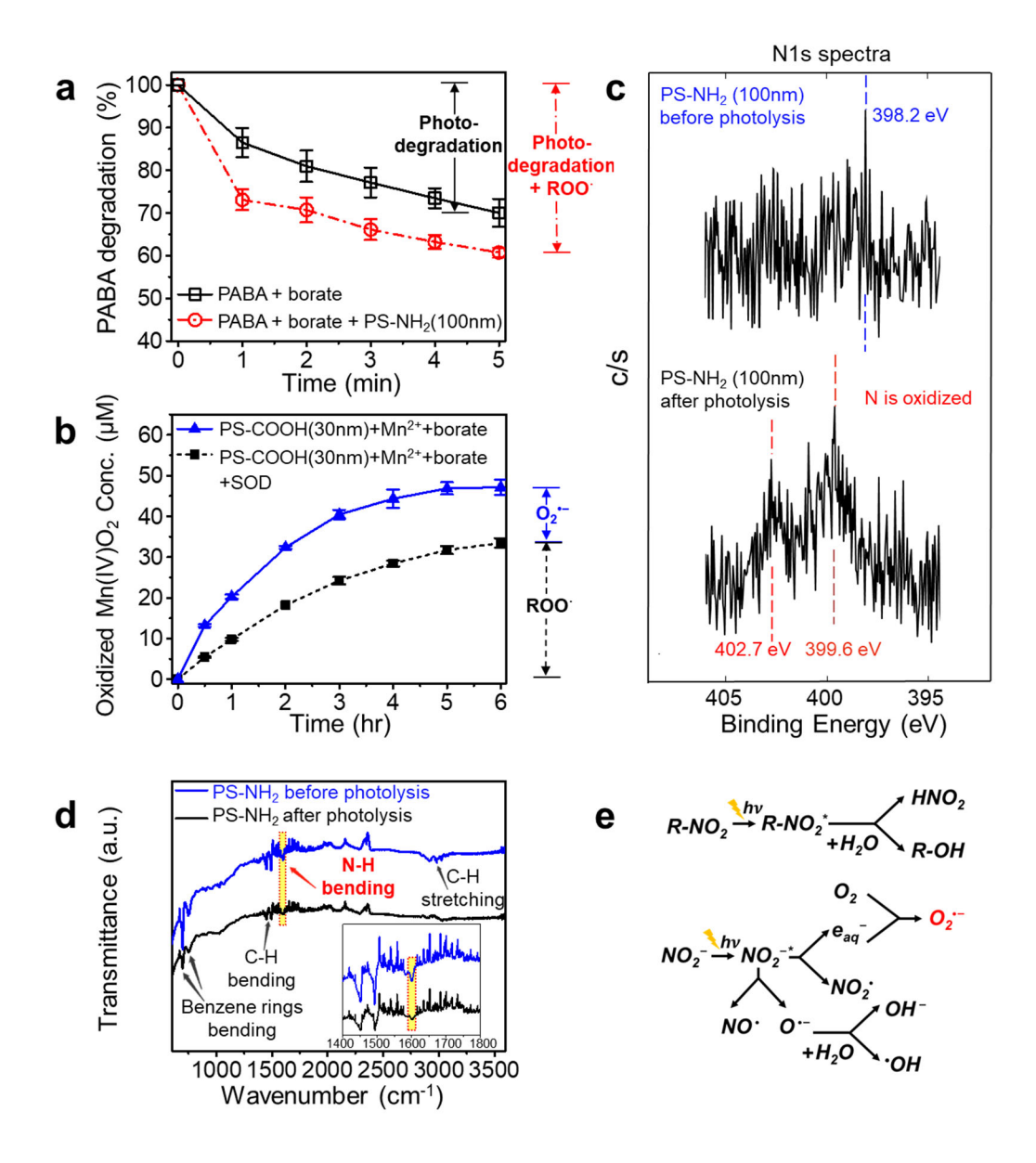
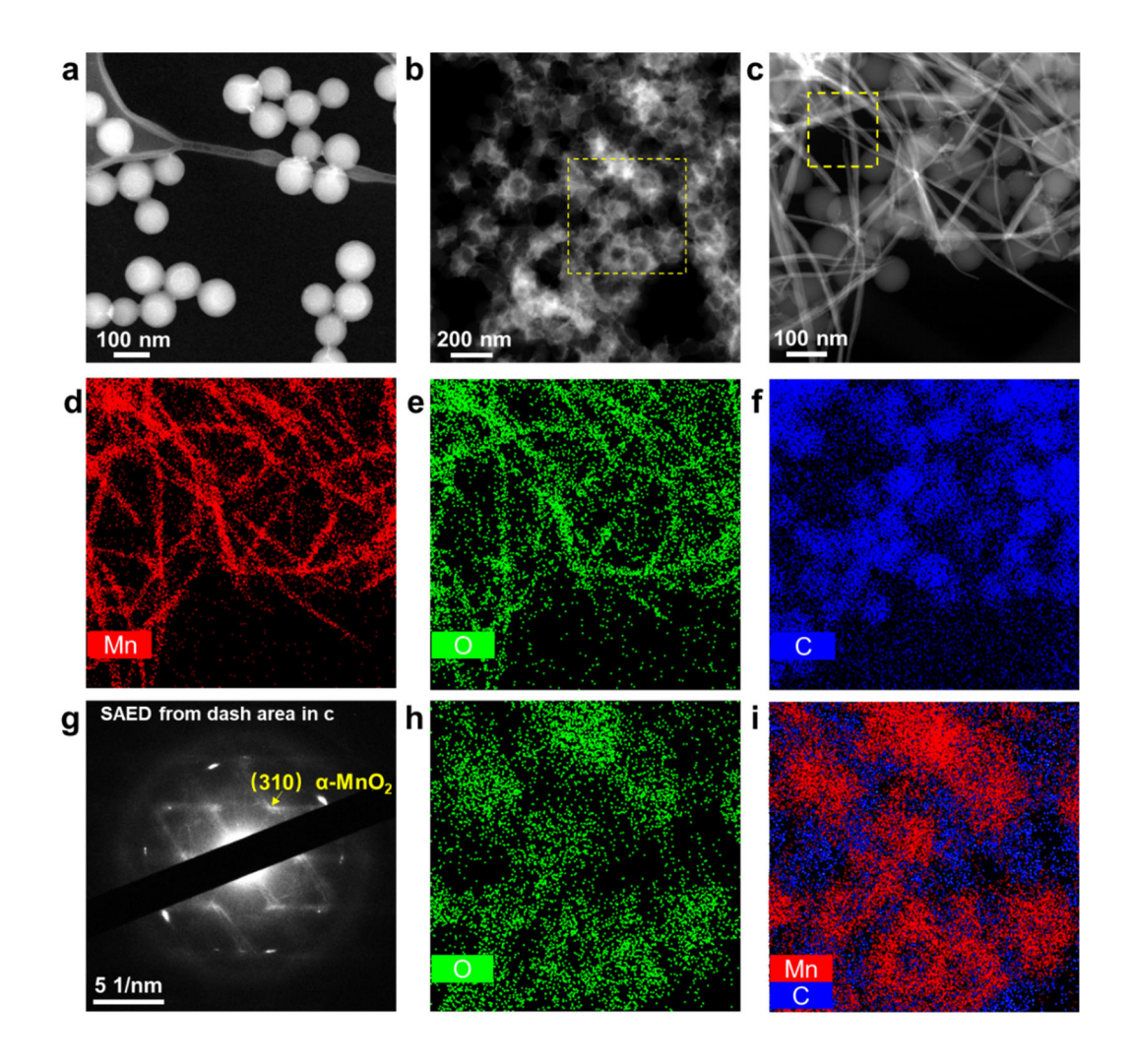
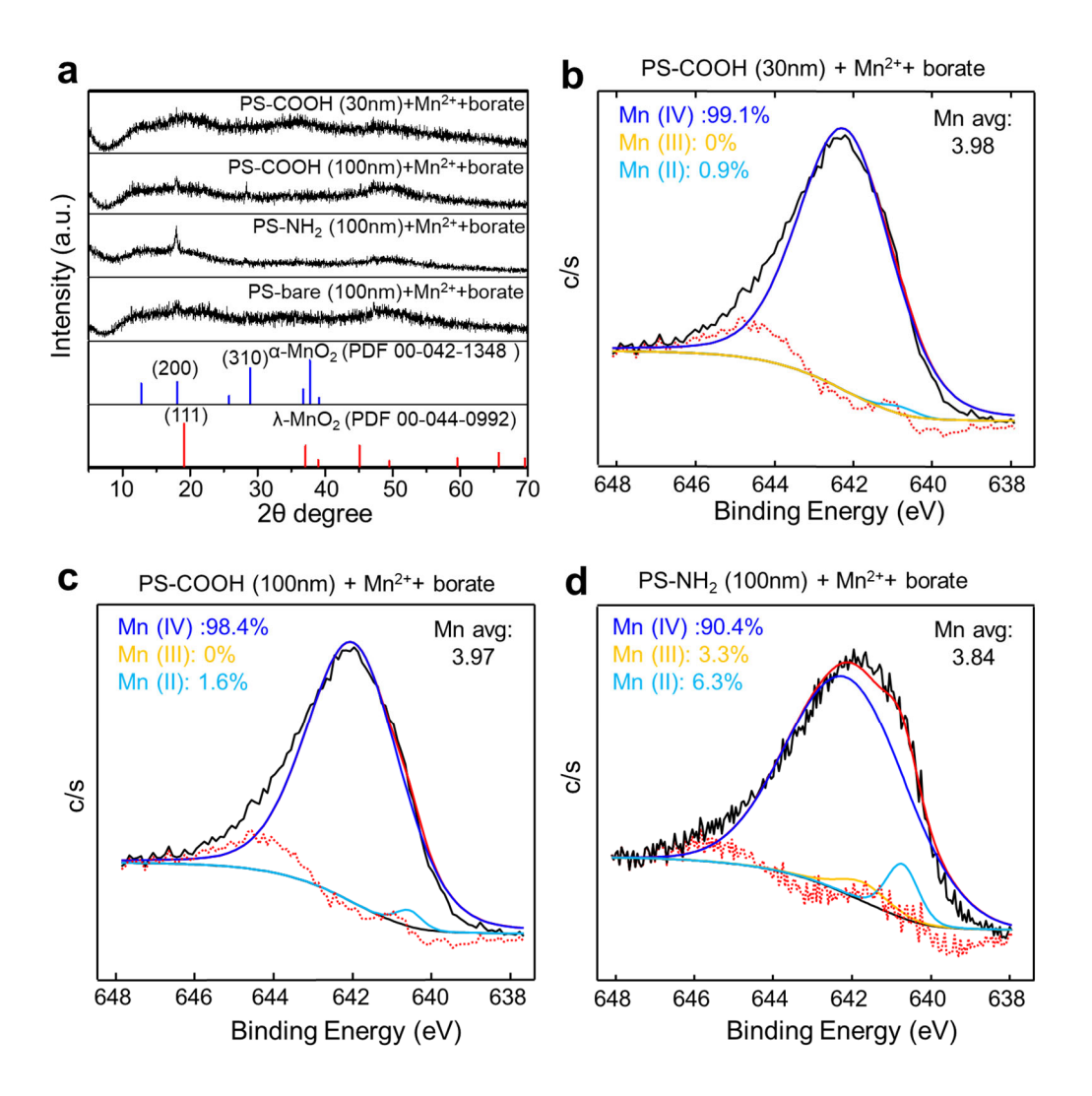


Figure 3. Mn<sup>2+</sup> Oxidation by ROO\* and O2\*. (a) Percent concentration decreases of PABA with/without 50 ppm of 100 nm PS-NH<sub>2</sub> over the elapsed experimental time under the conditions of 20 μM PABA and 10 mM borate buffer. (b) Oxidized Mn concentrations with/without 0.5 μM SOD with elapsed experimental time under the conditions of 0.1 mM MnCl<sub>2</sub>, 10 ppm of 30 nm PS-COOH, and 10 mM borate buffer. (c) XPS N1s spectra of PS-NH<sub>2</sub> nanoplastics before and after photolysis for 12 hr. (d) FTIR spectra of PS-NH<sub>2</sub>, before and after photolysis for 12 hr dried on a Si wafer. The same amount of PS-NH<sub>2</sub> solution was used for both cases. The FTIR spectra

were plotted without any normalization of peak intensities, thus the peaks can be semi-quantitatively compared. The peak indicating N-H bending is at 1602 cm<sup>-1</sup>. The zoomed-in image in the right corner shows the N-H bending peak weakened after photolysis. The upwards peaks at 2160 and 2364 cm<sup>-1</sup> are from the FTIR spectra of the Si wafer. The peaks at 697 and 749 cm<sup>-1</sup> are from benzene rings, the peaks at 1452 and 1485 cm<sup>-1</sup> correspond to C-H bending, and the peaks at 2980 and 3028 cm<sup>-1</sup> correspond to C-H stretching. The peaks of benzene rings and C-H also weakened because of the photochemical degradation of nanoplastics. (e) ROS generation pathways during photolysis of R-NO<sub>2</sub> and nitrite, provided by references 62 and 63. Error bars in (a–b) represent standard deviations from at least triplicate tests.



**Figure 4.** Morphologies of formed Mn oxide solids on 100 nm PS-COOH nanoplastics. Representative STEM images of (a) 100 nm PS-COOH nanoplastics without photolysis, and (b and c) Mn oxide solids formed by photolysis of a solution containing 0.1 mM MnCl<sub>2</sub>, 10 ppm of 100 nm PS-COOH, and 10 mM borate buffer after 6 hr. Images show different spots at different magnifications. (d–f) STEM-EDX elemental mapping of Mn, O, and C collected from (c). (g) SAED patterns from the dash area in (c), confirm the formation of α-MnO<sub>2</sub>. (h and i) STEM-EDX elemental mapping of O, Mn, and C collected from the dash area in (b), indicating Mn oxide solids formed surrounding the PS-COOH nanoplastics. For each condition, two TEM grids from duplicated tests were prepared and at least five different spots in each TEM grid were measured.



**Figure 5.** Comparison of crystalline phases and oxidation states of formed Mn oxide solids in the presence of different sizes and functional groups of nanoplastics. (a) HRXRD spectra of Mn oxide solids formed in four solutions: two solutions had different sizes of nanoplastics containing either 30 or 100 nm PS-COOH, 0.1 mM MnCl<sub>2</sub>, and 10 mM borate buffer; two more solutions had different functional groups of nanoplastics containing either 100 nm PS-NH<sub>2</sub> or PS-bare, 0.1 mM MnCl<sub>2</sub>, and 10 mM borate buffer. (b-d) The average Mn oxidation state of XPS Mn 2p<sub>3/2</sub> spectra calculated *via* Gaussian—Lorentzian fitting of Mn oxide solids formed under conditions of (b) 30 nm PS-COOH, (c) 100 nm PS-COOH, and (d) 100 nm PS-NH<sub>2</sub>. All solutions also contained 0.1 mM MnCl<sub>2</sub> and 10 mM borate buffer. At least duplicate tests were conducted for each experimental condition.